MULTI-PASS FERRITIC STEEL WELD MODELLING: PHASE TRANSFORMATION AND RESIDUAL STRESS

Y.L. SUN*, C.J. HAMELIN**, T.F. FLINT*, Q. XIONG*, A.N. VASILEIOU*, I. PANTELIS*, J.A. FRANCIS* and M.C. SMITH*

**School of Mechanical, Aerospace and Civil Engineering, The University of Manchester, M13 9PL, Manchester, UK, yongle.sun@manchester.ac.uk (Y.L. Sun)*
***Australian Nuclear Science and Technology Organisation, NSW 2234, Lucas Heights, Australia;* current affiliation: *EDF Energy, Gloucester, GL4 3RS, UK*

DOI 10.3217/978-3-85125-615-4-10

ABSTRACT

The solid state phase transformation (SSPT) occurring during welding thermal cycles gives rise to distinctive microstructures across the fusion zone and heat affected zone (HAZ), as well as significant effects on the residual stress generated in the weldment. We have developed a numerical model to simulate multi-pass welding in low alloy ferritic steel with consideration of SSPT. In this study, we applied a semi-empirical modelling approach to three-pass gas tungsten arc welding in a grooved plate made of SA508 steel (widely used in nuclear power plants). The microstructure, hardness and residual stress were predicted using a 2D finite element model and the predictions were compared with experimental results. We examined the sensitivity of the predicted hardness and stress to austenitisation kinetics and weld-metal plasticity. Two sets of empirical parameters were considered in the kinetic model of austenitisation to represent different levels of the heating-rate dependence of the critical temperatures (i.e. A_{c1} and A_{C3}) for austenite formation. A rule-of-mixtures method based on dilution and hardness was proposed to estimate the plastic properties of weld metal for each pass, using the predicted phase fractions and the yield stress dataset for each transformation product of base material. The modelling results show that the extent of the inter-critical HAZ, hardness and residual stress are affected by the austenitisation kinetics. The use of weld-metal plastic properties estimated by the rule-of-mixtures method can improve the residual stress prediction for the weld metal.

Keywords: Arc welding, phase transformation, microstructure, hardness, residual stress, modelling

INTRODUCTION

Weld-induced heterogeneous mechanical properties and residual stresses are two key factors affecting the performance and life of welded structures [1, 2]. Weld modelling has been playing an important role in the engineering design and structural integrity assessment of high-value and safety-critical weldments, such as those used in nuclear reactor pressure vessels [3, 4]. However, it is still challenging to accurately model multi-pass welding in

ferritic steel, which involves complicated metallurgical variation such as dilution, grain growth and solid state phase transformation (SSPT).

The impact of SSPT on weld residual stress has been confirmed in both experiments [5, 6] and modelling [7-9]. The effects of dilution, grain growth and inter-pass temperature on the microstructure and residual stresses in ferritic steel weldments have also been investigated experimentally and numerically [10-16]. Despite some key physics captured by the weld models, which are useful to establish qualitative understanding, the uncertainty in material parameters required by the models has been a serious issue when evaluating the prediction accuracy in a quantitative sense. In particular, the temperature- and microstructure-dependent properties of weld metal are notoriously difficult to measure, and consequently, estimation or approximation is usually needed to define the elastic-plastic model for weld metal. Ideally, the material properties for each phase (e.g. martensite, bainite or ferrite) of the weld metal should be individually determined by experimental tests. However, it is not feasible to produce samples for such tests. On one hand, the chemical compositions of the weld metals produced by different passes are normally different due to the chemical mismatch between the base and filler materials, as well as the dilution effect [10, 16, 17]. This implies that the weld-metal properties may differ from pass to pass, and a large matrix of tests is needed. On the other hand, tests must be performed on each phase of the unstressed weld metal to determine its evolutionary hardening behaviour for model definition purpose, rather than on the final hardened weld metal (potentially a mixture of different phases) present after the welding is complete. It is thus a daunting task to obtain material parameters for weld metal. Another issue causing uncertainty is the empirical parameters used in metallurgical models, such as the kinetic model of austenitisation that was proposed by Leblond and Devaux [18]. Dilatometry tests are a common method to experimentally determine the empirical parameters for phase transformation. However, in these tests, the temperature is strictly controlled to be uniform in the sample, while a steep temperature-gradient exists across the fusion zone (FZ) and heat affected zone (HAZ) of a weldment. Recent studies have demonstrated the effect of temperature gradient on metallurgical behaviour [19, 20]. Therefore, the metallurgical calibration tests may also need to take into account temperature gradient, which substantially increases the difficulty of experiment.

In this study, three-pass gas tungsten arc welding (GTAW) in a grooved SA508 steel plate is simulated using a thermal-metallurgical-mechanical finite element (FE) model. The sensitivity of the predictions for microstructure and residual stress to austenitisation kinetics and weld-metal plasticity is examined. We consider four analysis cases, i.e. two sets of empirical parameters are used in the kinetic model of austenitisation, and the plastic properties of each ferritic phase (e.g. martensite, bainite and ferrite) in the diluted weld metal for each pass are either assumed to be same as those for base material or estimated using a rule-of-mixtures method based on dilution and hardness.

MATERIALS AND METHODS

WELDING EXPERIMENT

A 200 × 150 × 20 mm plate made of a nuclear reactor pressure vessel steel, SA508 Gr.3 Cl.1, was used for the three-pass GTAW. The plate was grooved along the mid-width to a depth of 6 mm and at an angle of 45°, as shown in Fig. 1a and Fig. 1b. The welding parameters are given in Table 1. A SD3 filler wire with a diameter of 1.2 mm was used in weld bead deposition. Fig. 1c shows a transverse weld macrograph of the three-pass welded plate (half the weld is shown). To facilitate examination of the evolutionary metallurgical and mechanical response to welding, a single-pass plate was also produced using identical process parameters to the first pass of the three-pass weld. The chemical compositions of the base and filler materials are listed in Table 2, showing that the base material (C_{eq}=0.34) has a much higher hardenability than the filler material (C_{eq}=0.17).

Table 1 Gas tungsten arc welding parameters [21]

Pass	Voltage [V]	Current [A]	Torch speed [mm/min]	Wire feed rate [mm/min]	Nominal heat input [kJ/mm]
1	11.0	227	75	1000	2.0
2	11.5	217	75	1000	2.0
3	11.5	217	75	1000	2.0

Table 2 Chemical compositions (wt.%) of SA508 Gr.3 Cl.1 steel and SD3 filler metal [22]

	C	Si	Mn	Ni	Cr	Mo	V	Fe	C_{eq}
SA508 (base material)	0.2	0.25	1.4	0.8	0.2	0.5	0.003	Bal.	0.34
SD3 (filler material)	0.08	0.3	1.4	0.03	0.04	0.01	-	Bal.	0.17

Note: The Ito-Bessyo equation, i.e. $C_{eq}=C+Si/30+(Mn+Cu+Cr)/20+Ni/60+Mo/15+V/10+5B$ [23], is used to calculate the carbon equivalent C_{eq}.

WELD MODELLING

Thermal Model

The general purpose FE software Abaqus was employed to simulate the multi-pass welding, along with a series of user-defined subroutines to capture the thermal, metallurgical and mechanical response. The geometry and mesh of the FE weld model is shown in Fig. 1d. A 2D simplification [24] was adopted and one half of the welded plate was considered to take advantage of the symmetry of the geometry and process. The geometric profiles of the weld beads for the first and third passes were determined from the macrographs of the single-

pass and three-pass welded plates, respectively. The geometric profile of the weld bead for the second pass was inferred to ensure that the volume of the bead for each pass is same, since identical torch speed and wire feed rate were employed for all three passes (Table 1). The bead deposition was simulated via an "element birth and death" approach (i.e. "model change" in Abaqus [25]).

The thermal model was based on a 2D heat source which is equivalent to a 3D ellipsoidal heat source. A specialised weld modelling tool, FEAT-WMT [26], was used to derive the 2D heat source such that the 2D model predicts a transient temperature field identical to that on the cross-section of the plate under steady welding conditions, as modelled in 3D using FEAT-WMT. The thermal model comprises 1088 quadratic, quadrilateral elements (Abaqus element designation: DC2D8). Convection and radiation on plate surfaces were considered to an environment at 20 °C. The material parameters were obtained from Ref. [7].

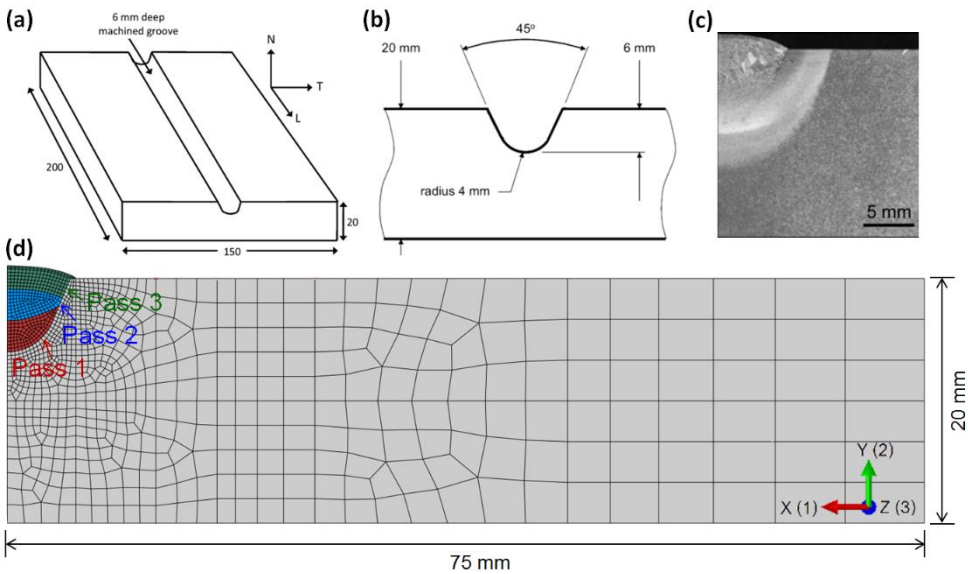

Fig. 1 Three-pass SA508 steel weldment and finite element model (X, Y and Z directions correspond to transverse, normal and longitudinal directions, respectively): (a) dimensions of grooved plate [22]; (b) transverse sectional profile [22]; (c) macrograph on transverse section (half part) [21]; (d) geometry and mesh of 2D weld model (half part).

Metallurgical Model

A semi-empirical approach was employed to model the reaction kinetics of austenite decomposition. The theoretical framework was initially established by Kirkaldy and Venugopalan [27] and later refined by Li et al. [28], based on which Hamelin et al. [7] have developed a weld model to predict the microstructure and residual stress in an autogenous edge-welded beam benchmark. The isothermal transformation for a ferritic phase is described by:

$$\tau(X,T) = \frac{F(\text{C, Mn, Si, Ni, Cr, Mo, } G)}{\Delta T^{m} \exp(-Q / RT)} S(X) \tag{1}$$

where τ is the transformation time required to form a fraction X of a ferritic phase (e.g. ferrite, pearlite or bainite); F is a function of the weight percentages of C, Mn, Si, Ni, Cr and Mo, as well as the ASTM number G of the prior austenite grain size (PAGS), see Table 3; $S(X)$ is a sigmoidal function; ΔT is undercooling and m is an empirical exponent; Q is the activation energy; T is absolute temperature; and R is the universal gas constant. The values of material parameters are shown in Table 3. For anisothermal transformation occurring during welding, a series of isothermal events are discretised and an additivity rule [7] is used to capture the kinetics. Empirical equations in terms of chemical composition are used to estimate the transformation start temperatures for ferrite, pearlite and bainite, see Ref. [7] for more details.

Table 3 Paramers [28] in the ferritic phase transormation model, i.e. Eq. (1)

Phase	*m*	*Q* [cal/mol ºC]	*F*(C, Mn, Si, Ni, Cr, Mo, *G*)
Ferrite	3	27500	exp (1.00+6.31C+1.78Mn+0.31Si+1.12Ni+2.70Cr+ 4.06Mo) / 2 $^{0.41G}$
Pearlite	3	27500	exp (-4.25+4.12C+4.36Mn+0.44Si+1.71Ni+3.33Cr+5.19√Mo)/2 $^{0.32G}$
Bainite	2	27500	exp(-10.23+10.18C+0.85Mn+0.55 Ni+0.90Cr+0.36Mo) / 2 $^{0.29G}$

The martensite transformation is modelled using the Koistinen-Marburger equation [29], i.e.

$$X_{\mathrm{M}} = X_{\mathrm{RA}}[1 - \exp(-A(M_{\mathrm{s}} - T))] \tag{2}$$

where X_{M} is the fraction of martensite, X_{RA} is the fraction of remaining austenite for martensitic transformation and A is a material parameter. The martensite start temperature for full austenite is estimated using an empirical linear equation of chemical composition [30]. Furthermore, the martensite start temperature is assumed to decrease linearly with the fractions of pre-formed ferritic phases, if any exist, before martensitic transformation [31].

Austenitisation kinetics are modelled using the Leblond-Devaux [18] approach, and the rate of austenite formation is expressed as

$$\dot{x} = \frac{x_{eq} - x}{\tau_{LD}} \tag{3}$$

where x_{eq} is the equilibrium austenite fraction and τ_{LD} is an empirical positive time constant. The parameter x_{eq} is assumed to increase from zero to one when temperature varies from 760 °C to 830 °C, which are the A_{c1} and A_{c3} temperatures, respectively, determined from dilatometry test data at low heating rates [31, 32]. Table 4 shows two cases of Leblond-Devaux model defined here, for which x_{eq} is taken to be same in both cases but the empirical parameter τ_{LD} is varied to represent different heating-rate sensitivity of the predicted austenitisation kinetics. It should be mentioned that the characteristic temperature of 1020°C for Case B is the estimated grain-coarsening temperature of SA508 steel [10].

For the FZ produced by each pass, 100% austenite formation is assumed when temperature drops below the melting temperature (T_m=1450 °C [7]).

Table 4 Two sets of parameters to define the Leblond-Devaux model for austenitisation kinetics

Temperature [°C]	Case A		Temperature [°C]	Case B	
	x_{eq}	τ_{LD} (s)		x_{eq}	τ_{LD} (s)
<760	0	1	<760	0	2
760	0	1	760	0	2
830	1	0.2	830	1	1.8
>830	1	0.05	1020	1	1.5
			>1020	1	0.05

Note: Linear interpolation is used between tabulated parameters at different temperatures.

Fig. 2 shows the predicted continuous heating transformation diagram for two cases of the austenitisation kinetics model defined using Eq. (3). The difference in the predicted austenitisation temperature ranges between Case A and Case B is negligible when the heating rate is lower than 1 °C/s, but it becomes significant when the heating rate is higher than 10 °C/s. The Case B model is more sensitive to heating rate than the Case A model, and thus it is expected that more extensive partial austenitisation will occur in the welding simulation using the Case B model.

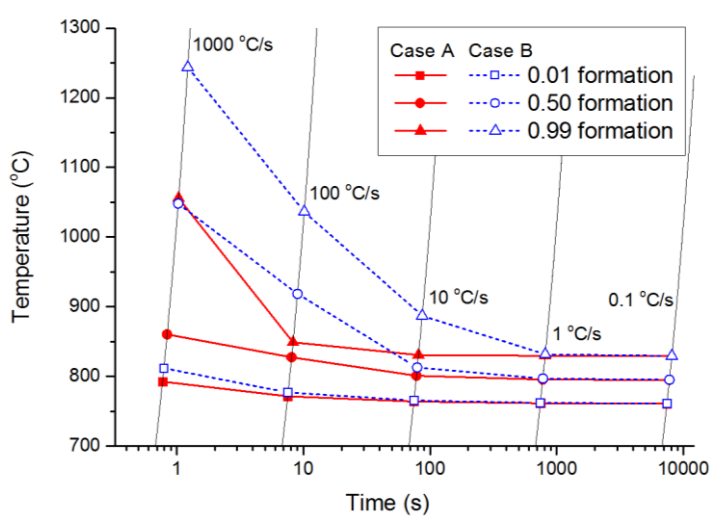

Fig. 2 Continuous heating transformation diagram for austenitisation kinetics predicted by Eq. (3) considering two cases of model definition (Table 4).

Austenite grain growth is modelled using the following equation [32]:

$$\frac{dL}{dt} = A\exp\left(-\frac{Q_g}{RT}\right)\left(\frac{1}{L}-\frac{1}{L_{lim}}\right) \quad (4)$$

where L is grain size, t is time, Q_g is activation energy, T is absolute temperature, R is the universal gas constant and L_{lim} is the limit of grain size due to pinning effect of precipitates [32]. The $1/L_{lim}$ term in Eq. (4) vanishes when the precipitates dissolve above the grain coarsening temperature of 1020 °C. For SA508 steel, Q_g = 190 kJ/mol, L_{lim} = 3 + 0.58(T-A_{c3}) in μm, and A is taken to be 4.2 μm^2/s and 16.8 μm^2/s for peak temperature below and above 1020 °C, respectively [16]. However, Eq. (4) is not applicable if peak temperature exceeds melting point during heating. In such a case, for simplicity, the PAGS is taken to be 0.4 mm, as an estimate in accordance with previous microscopic observations [22].

Empirical equations [33] are adopted to predict the Vickers micro-hardness of each ferritic phase, i.e.

$$Hv_M = 127 + 949\mathrm{C} + 27\mathrm{Si} + 11\mathrm{Mn} + 8\mathrm{Ni} + 16\mathrm{Cr} + 21\log(Vr) \tag{5}$$

$$Hv_B = -323 + 185\mathrm{C} + 330\mathrm{Si} + 153\mathrm{Mn} + 65\mathrm{Ni} + 144\mathrm{Cr} + 191\mathrm{Mo} + (89 + 53\mathrm{C} - 55\mathrm{Si} - 22\mathrm{Mn} - 10\mathrm{Ni} - 20\mathrm{Cr} - 33\mathrm{Mo})\log(Vr) \tag{6}$$

$$Hv_{F/P} = 42 + 223\mathrm{C} + 53\mathrm{Si} + 30\mathrm{Mn} + 12.6\mathrm{Ni} + 7\mathrm{Cr} + 19\mathrm{Mo} + (10 - 19\mathrm{Si} + 4\mathrm{Ni} + 8\mathrm{Cr} + 130\mathrm{V})\log(Vr) \tag{7}$$

for martensite, bainite and ferrite/pearlite, respectively; where the element symbol denotes the weight percentage of the chemical element and Vr (in °C /h) is the cooling rate at 700 °C.

The hardness of the mixture of different micro-constituents is calculated using a rule-of-mixtures as follows

$$Hv = Hv_M X_M + Hv_B X_B + Hv_{F/P}(X_F + X_P) + Hv_A X_A + Hv_{b0} X_{b0} \tag{8}$$

where X_M, X_B, X_F, X_P, X_A and X_{b0} are the fractions of martensite, bainite, ferrite, pearlite, austenite and base material, respectively. According to previous work [7, 10], we have Hv_{b0} = 200 and Hv_A = 160. The hardness of martensite, bainite and ferrite/pearlite is predicted by Eqs. (5), (6) and (7), respectively.

As the SSPT kinetics model and hardness prediction are primarily dependent on chemical composition, see Eqs. (1) and (5)-(7), it is necessary to take account of the chemical heterogeneity within the weldment. For weld metal, the content of each chemical element is calculated using a dilution-based rule-of-mixtures, i.e.

$$p_n = p_b D_n + p_f (1 - D_n) \tag{9}$$

where p_n is the content of the element for pass n; p_b and p_f are the contents of the element in the base and filler materials (Table 2), respectively; and D_n is the dilution for pass n. The dilution has been determined to be 0.44, 0.17 and 0.09 for the first, second and third passes, respectively [10].

Mechanical Model

The thermo-metallurgical deformation upon thermal cycling acts as the major driving force to generate stresses in the weldment. The total strain can be decomposed as follows

$$\varepsilon = \varepsilon_{\mathrm{e}} + \varepsilon_{\mathrm{p}} + \varepsilon_{\mathrm{th}} + \varepsilon_{\mathrm{tr}} + \varepsilon_{\mathrm{tp}} \tag{10}$$

where ε_{e}, ε_{p}, $\varepsilon_{\mathrm{th}}$, $\varepsilon_{\mathrm{tr}}$ and $\varepsilon_{\mathrm{tp}}$ are the elastic strain, plastic strain, thermal strain, metallurgical strain and transformation-induced plastic strain, respectively. On the right-hand side of Eq. (10), the third and fourth strain components are determined by the changes in temperature and phase, respectively. By contrast, the first two strain components are generated in conjunction with thermal-metallurgical deformation to satisfy the compatibility condition (i.e. internal constraint) implied in the continuum assumption, as well as the external constraint imposed, if any exists. The fifth strain component only arises in the presence of both SSPT and deviatoric stress.

In this study, the thermal strain and metallurgical strain were defined according to previous dilatometry test data on SA508 steel [7]. The dilation curve was decoupled between ferritic and austenitic phases, and a rule-of-mixtures was employed to estimate the individual contribution from the ferritic and austenitic phases. The transformation-induced plastic strain is calculated using the following constitutive equation [34]

$$\dot{\varepsilon}_{ij}^{tp} = \frac{3}{2} K s_{ij} f'(z) \dot{z} \tag{11}$$

where $\dot{z}$ is the rate of phase transformation, $f(z)$ is a normalised function, s_{ij} is the deviatoric stress, and K is a material constant. For SA508 steel, we assume that $f(z) = z(2-z)$ and $K = 10^{-4}$ MPa^{-1} [34].

The FE mesh of the mechanical model is same as that of the thermal model, except that quadratic, quadrilateral, generalised plane strain and hybrid elements (Abaqus designation: CPEG8H) were used in the mechanical model. The bottom corner node on the symmetry plane was fully fixed, while only displacement constraint in the X direction (i.e. U1 = 0) was imposed on the whole symmetry plane.

The elasto-plastic properties are dependent on both temperature and microstructure, and the material parameters reported in Ref. [7] were adopted for base material and its transformation products. No plastic property dataset is available for the filler material, so a scaling method is developed to make an approximation. Since yield strength is generally proportional to hardness [35], the yield stress for each ferritic phase of the filler material can be estimated using the filler-to-base ratio of calculated hardness and the plastic property dataset for each ferritic phase of the base material. Table 5 shows the calculated hardness using Eqs. (5)-(7) and the corresponding hardness ratio (i.e. scaling ratio).

Table 5 Vickers hardness for each ferritic phase of base/filler material

	Martensite	Bainite	Ferrite/pearlite
Base material	453.3	319.4	214.9
Filler material	332.0	236.6	142.2
Filler-to-base ratio	0.73	0.74	0.66

Note: Hardness is calculated using Eqs. (5)-(7) wherein cooling rate is taken to be 27 ^{o}C/s according to the thermal modelling result [10].

For weld metal corresponding to each pass, a dilution-based rule-of-mixtures method was employed to estimate the contribution from both base and filler materials to the plastic behaviour of the weld metal, as illustrated in Fig. 3. Table 6 shows the different modelling scenarios considered in the mechanical analysis, with regard to different definitions of austenitisation kinetics and plastic property.

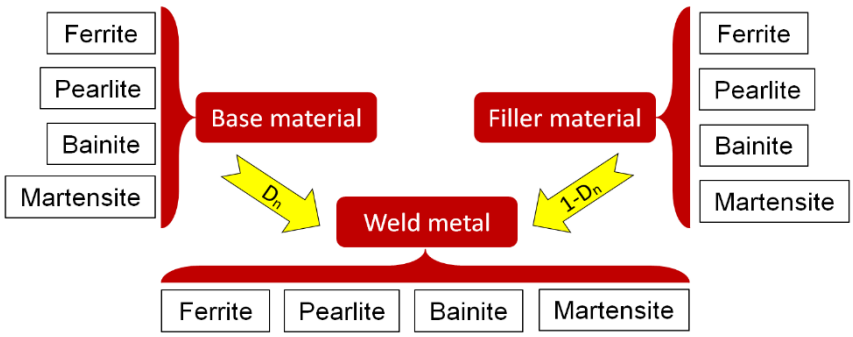

Fig. 3 Illustration of the dilution-based rule-of-mixtures estimation of plastic properties of weld-metal.

Table 6 Modelling Scenarios for mechanical analysis

Model No.	Austenitisation case	Yield stress scaling
1	A	No
2	B	No
3	A	Yes
4	B	Yes

RESULTS AND DISCUSSION

MICROSTRUCTURE AND HARDNESS

Our previous study [10] has shown a good accuracy of the temperature prediction by the weld model, as verified by thermocouple data and FZ/HAZ observations. Here, particular attention is paid to the heating during which austenitisation occurs. Heating rates were calculated at 700 °C for material points experiencing peak temperatures higher than 700 °C, and the averaged heating rates are 169±56 °C/s, 146±53 °C/s and 122±42 °C/s for the

first, second and third passes, respectively, based on the thermal solution of the weld model. According to Fig. 2, the difference in the predicted austenitisation kinetics between Case A and Case B (Table 4) is significant for the heating rates larger than 100 °C/s, which is similar to those involved in the simulated welding. Therefore, unsurprisingly, a much wider inter-critical HAZ (ICHAZ, i.e. partially austenitised zone) is predicted in Case B, as shown in Fig. 4. This is because the empirical time constant, i.e. $\tau_{LD,}$ adopted in Case B is larger than that in Case A, and the τ_{LD} dictates the retardation effect during austenitisation.

Fig. 5 and Fig. 6 show the predicted fractions of different ferritic phases (i.e. bainite, martensite and ferrite) for austenitisation Case A and Case B, respectively. For base material HAZ, a mixture of bainite and martensite is formed in the coarse-grained HAZ (CGHAZ, adjacent to FZ boundary), while bainite is dominant in the fine-grained HAZ (FGHAZ, relatively far from FZ boundary). For as-deposited weld metal, the fraction of martensite is considerable after first pass, but it became minor when more passes were deposited; in the reheated weld metal (i.e. HAZ formed in previous FZ), bainite is the major constituent predicted and some ferrite is also present. It is noted that, different microstructures are predicted in the weld metal and the base material, particularly for the CGHAZ, although similar temperature histories are involved. The difference is due to the chemical heterogeneity as controlled by the dilution for each pass, see Eq. (9), given the chemical mismatch between the base and filler materials (Table 2). These predicted microstructures are overall consistent with microscopic observations in experiment, except that acicular ferrite was present in the actual weld metal but it has not been explicitly considered (i.e. acicular ferrite is treated being equivalent to bainite) in the weld model; more discussion about this issue can be found in our previous work [10].

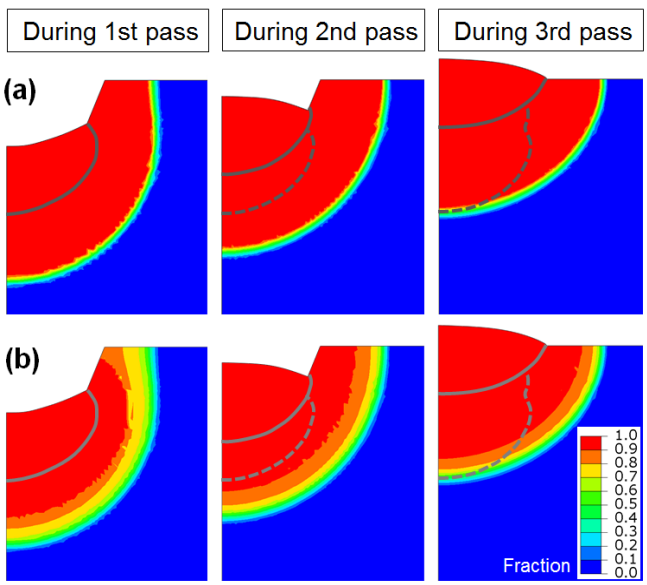

Fig. 4 Predicted distributions of maximum fractions of austenite formed during each pass: (a) austenitisation Case A; (b) austenitisation Case B. Note that the solid and dashed grey lines indicate the current and accumulated fusion boundaries, respectively.

Here, we focus on the effect of austenitisation kinetics on the final microstructure. The effect is pronounced for bainite (Figs. 5a and 6a) and discernible for ferrite (Figs. 5c and 6c), but negligible for martensite (Figs. 5b and 6b). This is because the difference in austenitisation kinetics mainly affects the ICHAZ which is adjacent to the FGHAZ where bainite is dominant, ferrite is present (only in reheated weld metal) but martensite is absent. In other words, in the ICHAZ, the base material or the preceding transformation products persist, and hence the fraction of newly transformed phase (mainly bainite) is limited. In the austenitisation Case B, a more extensive ICHAZ develops (Fig. 4), and consequently, markedly less bainite and slightly less ferrite are formed, in comparison with the austenitisation Case A, as shown in Figs. 5 and 6.

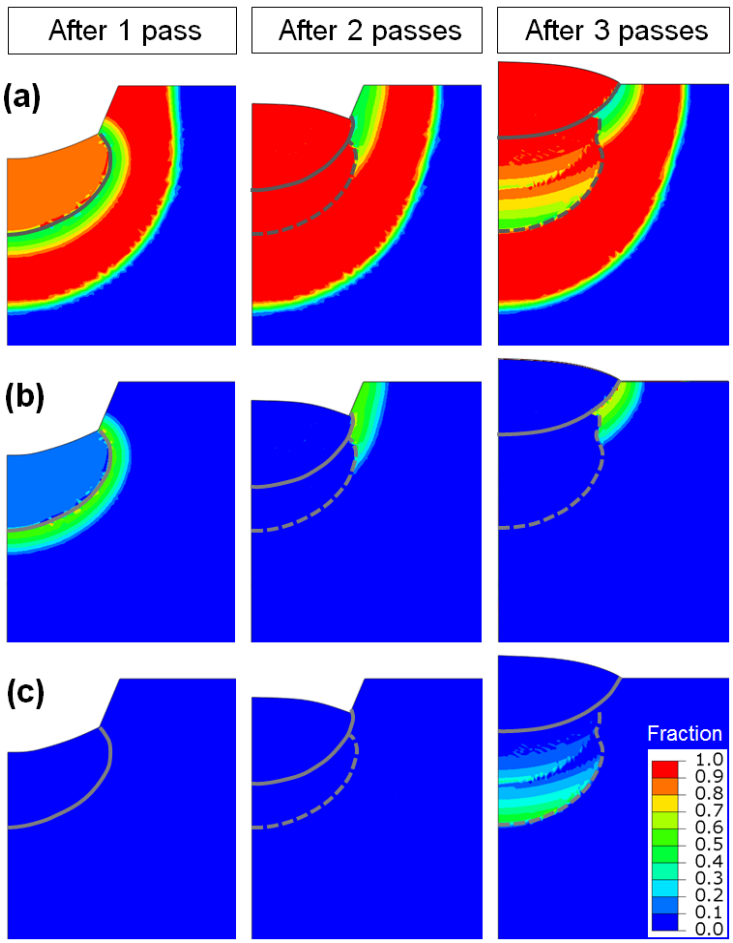

Fig. 5 Predicted distributions of ferritic phase fractions (austenitisation Case A) after different number of passes: (a) bainite; (b) martensite; (c) ferrite. Note that the solid and dashed grey lines indicate the current and accumulated fusion boundaries, respectively.

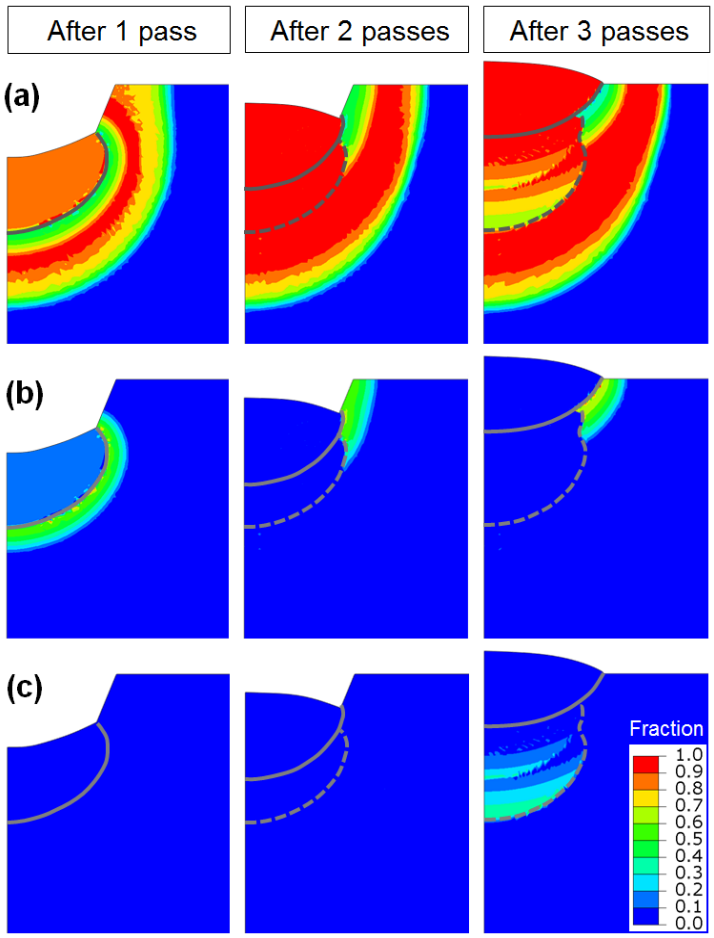

Fig. 6 Predicted distributions of ferritic phase fractions (austenitisation Case B) after different number of passes: (a) bainite; (b) martensite; (c) ferrite. Note that the solid and dashed grey lines indicate the current and accumulated fusion boundaries, respectively.

Fig. 7 shows the comparison between the predicted and measured hardness distributions. It is evident that a better agreement is achieved in the austenitisation Case B. The narrower ICHAZ (consequently, wider FGHAZ) formed in the austenitisation Case A leads to a significant overestimate of hardness close to the base material, in contrast to the lower hardness found in the wider ICHAZ formed in the austenitisation Case B. Similar results were also obtained by Hamelin et al. [36]. For both Case A and Case B, the hardness in the reheated weld metal is underestimated (Fig. 7c), due to a considerable fraction of ferrite predicted therein (Figs. 5c and 6c). This may indicate an overestimate of ferrite in the reheated weld metal. It is also noted that Case B assumption somewhat reduces the underestimation of hardness in the reheated weld metal (Fig. 7c), implying that more significant retardation of austenitisation may also occur in the weld metal. As re-austenitisation and grain growth in columnar-grained weld metal is complicated, a more sophisticated model may be needed to capture the exact metallurgical behaviour, opening a direction for future work.

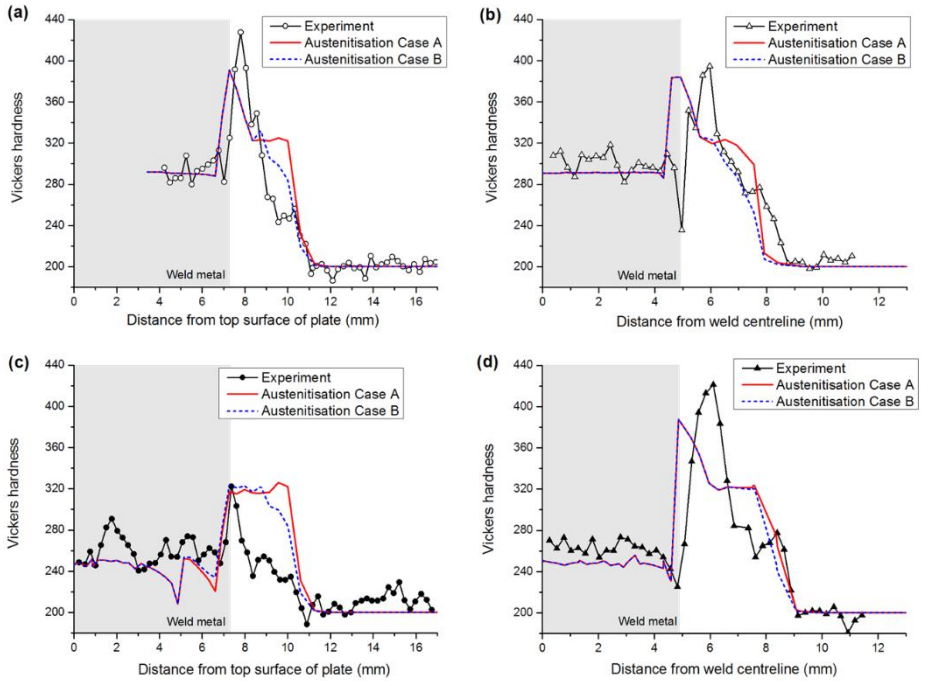

Fig. 7 Predicted and measured hardness distributions: (a) through-thickness distribution after one pass; (b) transverse distribution after one pass; (c) through-thickness distribution after three passes; (d) transverse distribution after three passes. The hardness measurement results are taken from the Ref. [22]. Note that the transvers distributions are examined at depths of 4.5 mm and 2.0 mm to the top surface after one pass and three passes, respectively.

RESIDUAL STRESS

Fig. 8 compares the predicted and measured residual stress distributions through thickness, as well as the predictions between different modelling scenarios. Good agreement is achieved for transverse stress after one pass, while for other cases the predictions are less accurate and only have a qualitative agreement. It is believed that the inaccuracy is mainly caused by the longitudinal over-constraint under generalised plane strain assumption and the uncertainty in weld-metal material properties adopted in the mechanical model, which have more significant effects when more weld beads are deposited. In addition, experimental observations show a significant presence of acicular ferrite in the weld metal [22], which has not been explicitly considered in the current metallurgical model, hence limiting the accuracy of the predicted SSPT kinetics.

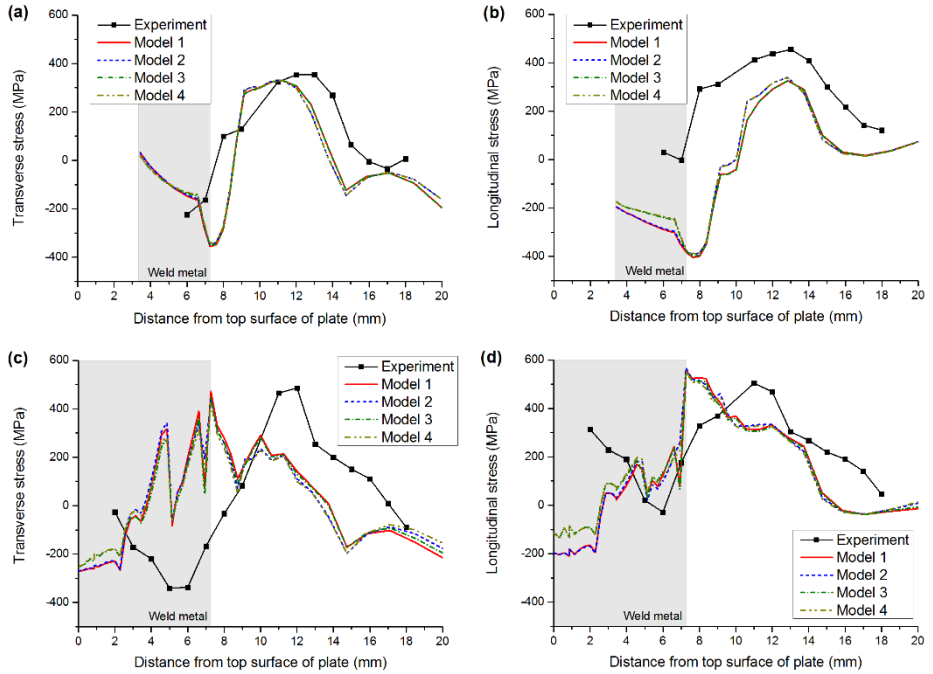

Fig. 8 Predicted and measured through-thickness distributions of residual stresses: (a) transverse stress after one pass; (b) longitudinal stress after one pass; (c) transverse stress after three passes; (d) longitudinal stress after three passes. The neutron diffraction stress measurement results are taken from Ref. [22]. The different modelling scenarios are described in Table 6.

The difference between the four modelling scenarios (Table 6) is more pronounced for longitudinal stresses than for transverse stresses. The different austenitisation kinetics (i.e. Case A and Case B) primarily affect the stress level in the ICHAZ and the adjacent base material. The prediction of stresses in the weld metal has been slightly improved in modelling scenarios 3 and 4 wherein the rule-of-mixtures method based on pass-by-pass dilution is used to estimate the distinctive yield stress in the weld metal.

Fig. 9 and Fig. 10 show the contours of longitudinal and transverse stresses, respectively, after three passes. The results further confirm that the different cases of austenitisation kinetics model (Table 4) have discernible but overall insignificant effect on the residual stresses. By contrast, the effect of weld-metal yield stress is more considerable, particularly in the FZ produced by the third pass. The plastic properties of the weld metal are expected to be more complicated than that approximated using simple rule-of-mixtures, and thus more significant difference in residual stress prediction may be expected if more accurate plastic constitutive parameters are used.

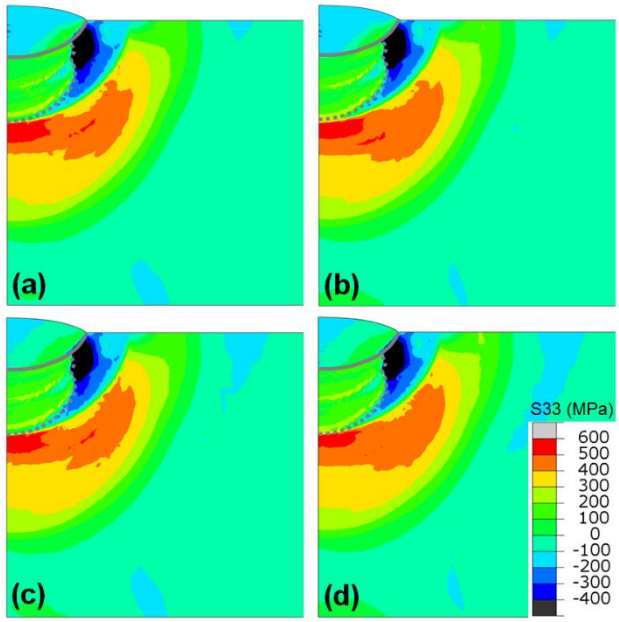

Fig. 9 Predicted distributions of longitudinal stress after three passes: (a) Model 1; (b) Model 2; (c) Model 3; (d) Model 4.

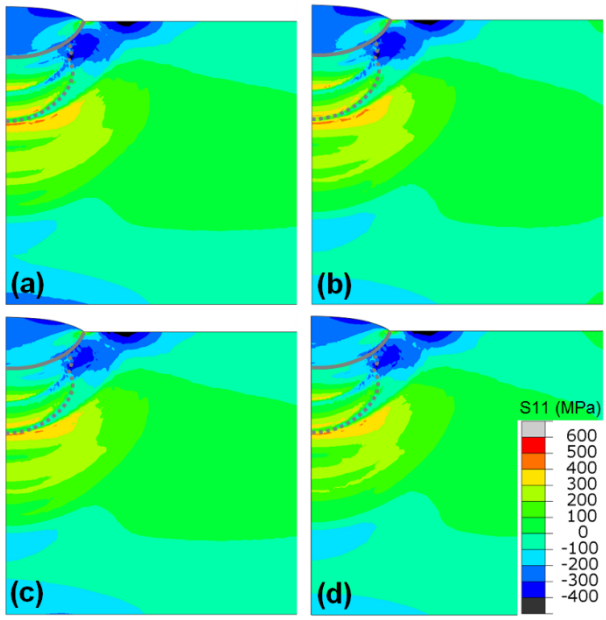

Fig. 10 Predicted distributions of transverse stress after three passes: (a) Model 1; (b) Model 2; (c) Model 3; (d) Model 4.

CONCLUSIONS

Three-pass gas tungsten arc welding in a grooved plate made of a low alloy ferritic steel (SA508 Gr.3 Cl.1) has been modelled with consideration of solid state phase transformation. The analysis focused on the sensitivity of the predicted microstructure, hardness and residual stress to the empirical parameter in the austenitisation kinetics model and the assumed yield stress of the weld metal. Four modelling scenarios have been examined (Tables 4 and 6). The numerical predictions were also compared with experimental measurements.

The modelling results show that a stronger heating-rate dependence of A_{c1} and A_{c3} temperatures leads to a wider ICHAZ; and consequently, in the ICHAZ, the austenitisation kinetics markedly affects the microstructure and hardness, while only slightly affects the residual stress. The approximation of weld-metal plastic properties using dilution-based rule-of-mixtures method can improve the residuals stress prediction for the weld metal, but the accuracy is still limited due to other issues (e.g. 2D simplification and acicular ferrite transformation). Future work will be devoted to more accurate material properties and SSPT kinetics for weld metal in a 3D model.

ACKNOWLEDGEMENTS

The authors gratefully acknowledge the funding support from EPSRC grant EP/J021172/1, for the development and characterisation of welds under the NNUMAN programme. The assistance given by the IT Services and the use of the Computational Shared Facility at the University of Manchester are also acknowledged.

REFERENCES

[1] S. KOU. Welding metallurgy, John Wiley & Sons, New Jersey, 2003.
[2] J.A. Goldak, M. Akhlaghi. Computational welding mechanics, Springer Science & Business Media, 2006.
[3] J.A. FRANCIS, H.K.D.H. BHADESHIA, P.J. WITHERS. Welding residual stresses in ferritic power plant steels, Materials Science and Technology 23 (2007) 1009-1020.
[4] Y. RONG, J. XU, Y. HUANG, G. ZHANG. Review on finite element analysis of welding deformation and residual stress, Science and Technology of Welding and Joining 23 (2018) 1-11.
[5] J.A. FRANCIS, H.J. STONE, S. KUNDU, H.K.D.H. BHADESHIA, R.B. ROGGE, P.J. WITHERS, L. KARLSSON. The Effects of Filler Metal Transformation Temperature on Residual Stresses in a High Strength Steel Weld, Journal of Pressure Vessel Technology 131 (2009) 041401-041408.
[6] S.W. OOI, J.E. GARNHAM, T.I. RAMJAUN. Review: Low transformation temperature weld filler for tensile residual stress reduction, Materials & Design 56 (2014) 773-781.
[7] C.J. HAMELIN, O. MURÁNSKY, M.C. SMITH, T.M. HOLDEN, V. LUZIN, P.J. BENDEICH, L. EDWARDS. Validation of a numerical model used to predict phase distribution and residual stress in ferritic steel weldments, Acta Materialia 75 (2014) 1-19.
[8] A.N. VASILEIOU, M.C. SMITH, J. BALAKRISHNAN, J.A. FRANCIS, C.J. HAMELIN. The impact of transformation plasticity on the electron beam welding of thick-section ferritic steel components, Nuclear Engineering and Design 323 (2017) 309-316.

[9] D. DENG, H. MURAKAWA. Prediction of welding residual stress in multi-pass butt-welded modified 9Cr–1Mo steel pipe considering phase transformation effects, Computational Materials Science 37 (2006) 209-219.
[10] Y. SUN, C.J. HAMELIN, M.C. SMITH, A.N. VASILEIOU, T.F. FLINT, J.A. FRANCIS. Modelling of dilution effects on microstructure and residual stress in a multi-pass weldment. ASME 2018 Pressure Vessels and Piping Conference. Prague, Czech Republic: American Society of Mechanical Engineers, 2018.
[11] T. RAMJAUN, H. STONE, L. KARLSSON, J. KELLEHER, S. OOI, K. DALAEI, J. REBELO KORNMEIER, H. BHADESHIA. Effects of dilution and baseplate strength on stress distributions in multipass welds deposited using low transformation temperature filler alloys, Science and Technology of Welding and Joining 19 (2014) 461-467.
[12] T. RAMJAUN, H. STONE, L. KARLSSON, J. KELLEHER, R. MOAT, J.R. KORNMEIER, K. DALAEI, H. BHADESHIA. Effect of interpass temperature on residual stresses in multipass welds produced using low transformation temperature filler alloy, Science and Technology of Welding and Joining 19 (2014) 44-51.
[13] H. DAI, R. MOAT, P. WITHERS. Modelling the interpass temperature effect on residual stress in low transformation temperature stainless steel welds. ASME 2011 Pressure Vessels and Piping Conference: American Society of Mechanical Engineers, 2011. p.1451-1458.
[14] Y. SUN, C.J. HAMELIN, M.C. SMITH, L. EDWARDS. Predicting an optimal inter-pass temperature to mitigate residual stress and distortion in ferritic steel weldments. ASME Pressure Vessels and Piping Conference. Vancouver, Canada, 2016.
[15] C.J. HAMELIN, O. MURÁNSKY, L. EDWARDS. The Influence of Austenite Grain Size during Welding Simulations of Ferritic Steels, Advanced Materials Research 996 (2014).
[16] Y.L. SUN, G. OBASI, C.J. HAMELIN, A.N. VASILEIOU, T.F. FLINT, J. BALAKRISHNAN, M.C. SMITH, J.A. FRANCIS. Effects of dilution on alloy content and microstructure in multi-pass steel welds, Journal of Materials Processing Technology 265 (2019) 71-86.
[17] J.N. DUPONT, A.R. MARDER. Dilution in single pass arc welds, Metallurgical and Materials Transactions B 27 (1996) 481-489.
[18] J.B. LEBLOND, J. DEVAUX. A new kinetic model for anisothermal metallurgical transformations in steels including effect of austenite grain size, Acta Metallurgica 32 (1984) 137-146.
[19] T.F. FLINT, C. PANWISAWAS, Y. SOVANI, M.C. SMITH, H.C. BASOALTO. Prediction of grain structure evolution during rapid solidification of high energy density beam induced re-melting, Materials & Design 147 (2018) 200-210.
[20] S. CHAKRABORTY, P. KUMAR, A. CHOUDHURY. Phase-field modeling of grain-boundary grooving and migration under electric current and thermal gradient, Acta Materialia 153 (2018) 377-390.
[21] B.M. PELLEREAU, C.M. GILL, M. DAWSON, P.R. HURRELL, J. FRANCIS, A. MARK. Finite element modelling and measurements of residual stress and phase composition in ferritic welds. ASME 2010 Pressure Vessels and Piping Division/K-PVP Conference: American Society of Mechanical Engineers, 2010. p.1385-1392.
[22] A. MARK, J. FRANCIS, H. DAI, M. TURSKI, P. HURRELL, S. BATE, J. KORNMEIER, P. WITHERS. On the evolution of local material properties and residual stress in a three-pass SA508 steel weld, Acta Materialia 60 (2012) 3268-3278.
[23] Ş. TALAŞ. The assessment of carbon equivalent formulas in predicting the properties of steel weld metals, Materials & Design 31 (2010) 2649-2653.
[24] S. SARKANI, V. TRITCHKOV, G. MICHAELOV. An efficient approach for computing residual stresses in welded joints, Finite Elements in Analysis and Design 35 (2000) 247-268.
[25] Dassault Systèmes, ABAQUS Analysis User's Manual, (v6.13 Documentation).
[26] R. SMITH. FEAT-WMT: Weld-modelling tool user guide, FEATWMT: weld-modelling tool user guide: FeatPlus Limited (2010).
[27] J. KIRKALDY, D. VENUGOPALAN. Prediction of microstructure and hardenability in low-alloy steels, Phase Transformations in ferrous alloys (1983) 125-148.
[28] M.V. LI, D.V. NIEBUHR, L.L. MEEKISHO, D.G. ATTERIDGE. A computational model for the prediction of steel hardenability, Metallurgical and Materials transactions B 29 (1998) 661-672.

[29] D.P. KOISTINEN, R.E. MARBURGER. A general equation prescribing the extent of the austenite-martensite transformation in pure iron-carbon alloys and plain carbon steels, Acta Metallurgica 7 (1959) 59-60.
[30] C. KUNG, J. RAYMENT. An examination of the validity of existing empirical formulae for the calculation of Ms temperature, Metallurgical Transactions A 13 (1982) 328-331.
[31] N. O'MEARA, H. ABDOLVAND, J.A. FRANCIS, S.D. SMITH, P.J. WITHERS. Quantifying the metallurgical response of a nuclear steel to welding thermal cycles, Materials Science and Technology (2016) 1-16.
[32] H. POUS-ROMERO, I. LONARDELLI, D. COGSWELL, H.K.D.H. BHADESHIA. Austenite grain growth in a nuclear pressure vessel steel, Materials Science and Engineering: A 567 (2013) 72-79.
[33] P. MAYNIER, J. DOLLET, P. BASTIEN. Creusot-Loire system for the prediction of the mechanical properties of low alloy steel products. in: Doane DV, Kirkaldy JS, (Eds.). Hardenability concepts with applications to steels. The Metallurgical Society of AIME, Warrendale, Pennsylvania, 1978. pp. 518-545.
[34] J.-B. LEBLOND, G. MOTTET, J. DEVAUX, J.-C. DEVAUX. Mathematical models of anisothermal phase transformations in steels, and predicted plastic behaviour, Materials science and technology 1 (1985) 815-822.
[35] E.J. PAVLINA, C.J. VAN TYNE. Correlation of Yield Strength and Tensile Strength with Hardness for Steels, Journal of Materials Engineering and Performance 17 (2008) 888-893.
[36] C.J. HAMELIN, O. MURÁNSKY, P. BENDEICH, K. SHORT, L. EDWARDS. Predicting solid-state phase transformations during welding of ferritic steels. Materials Science Forum, vol. 706: Trans Tech Publ, 2012. p.1403-1408.